Observation-Consistent Input and Whitecapping Dissipation in a Model for Wind-Generated Surface Waves: Description and Simple Calculations

W. ERICK ROGERS

Oceanography Division, Naval Research Laboratory, Stennis Space Center, Mississippi

ALEXANDER V. BABANIN

Faculty of Engineering and Industrial Science, Swinburne University of Technology, Melbourne, Victoria, Australia

DAVID W. WANG

Oceanography Division, Naval Research Laboratory, Stennis Space Center, Mississippi

(Manuscript received 25 May 2011, in final form 30 December 2011)

ABSTRACT

A new wind-input and wind-breaking dissipation for phase-averaged spectral models of wind-generated surface waves is presented. Both are based on recent field observations in Lake George, New South Wales, Australia, at moderate-to-strong wind-wave conditions. The respective parameterizations are built on quantitative measurements and incorporate new observed physical features, which until very recently were missing in source terms employed in operational models. Two novel features of the wind-input source function are those that account for the effects of full airflow separation (and therefore relative reduction of the input at strong wind forcing) and for nonlinear behavior of this term. The breaking term also incorporates two new features evident from observational studies; the dissipation consists of two parts—a strictly local dissipation term and a cumulative term—and there is a threshold for wave breaking, below which no breaking occurs. Four variants of the dissipation term are selected for evaluation, with minimal calibration to each. These four models are evaluated using simple calculations herein. Results are generally favorable. Evaluation for more complex situations will be addressed in a forthcoming paper.

1. Introduction

Over the past four decades, the wave forecast is routinely conducted by means of spectral numerical modeling of physical processes responsible for wave development and wave evolution. The evolution of the wave spectrum is described by means of the radiative transfer equation, which in deep water can be written as

$$\frac{\partial N}{\partial t} + \nabla \cdot \mathbf{c}N = \frac{S_{\text{tot}}}{\sigma} = \frac{S_{\text{in}} + S_{\text{ds}} + S_{\text{nl}}}{\sigma}, \qquad (1)$$

where $N = N(\sigma, \theta, \mathbf{x}, t)$ is the wave action density spectrum dependent on angular frequency σ from a frame of reference relative to any local currents, wave direction θ, distance vector $\mathbf{x}$, and time t; c is the energy propagation velocity of the waves in each dimension; S_{tot} represents all energy fluxes contributing to wind-wave evolution; and the action density is related to the energy density as simply $N = E/\sigma$. In deep water, it is generally accepted that wind-wave growth is primarily a result of three physical processes: atmospheric input from the wind to the waves S_{in}, wave dissipation (resulting from breaking and interaction with turbulence and viscosity) S_{ds}, and nonlinear energy transfer between the wave components S_{nl}. In finite depths, additional terms resulting from wave-bottom friction and triad interactions become significant, and more terms can be formulated, which may become important in particular circumstances. All of these source terms are spectral functions. The reader is referred to The WISE Group (2007) for a more complete overview of this technique of wave modeling.

The input and whitecapping source terms used in this paper are based on observational studies described by

Corresponding author address: W. Erick Rogers, Oceanography Division, Code 7322, Naval Research Laboratory, Stennis Space Center, MS 39529.
E-mail: erick.rogers@nrlssc.navy.mil

DOI: 10.1175/JTECH-D-11-00092.1

Banner et al. (2000), Babanin et al. (2001), Young and Babanin (2006, hereafter YB06), Donelan et al. (2006, hereafter DBYB), and others. Quantitatively, the wind input is developed from direct measurement of surface elevation and pressure in field conditions, which can be expressed in terms of fractional energy increase (Donelan et al. 2005). Qualitatively, there are physical features of behavior of both the input and breaking dissipation observed in these studies, but at present these features are still finding their way into operational modeling. Two novel features of the wind-input source function are those that account for the effects of airflow separation (and therefore relative reduction of the input at strong wind forcing) and for the nonlinear behavior of this term (Donelan et al. 2005; DBYB). The whitecapping-dissipation term also incorporates two new features evident from observational studies—the dissipation is a two-phase function, that is, it consists of two parts, a strictly local dissipation term and a cumulative term at smaller scales (higher frequencies), and there is a threshold for wave breaking below which no breaking occurs (Banner et al. 2000; Babanin et al. 2001; Babanin and Young 2005, hereafter BY05; YB06; Babanin, 2009).

How are these physics included in the spectral-model source terms up to date? In Wavewatch III (Tolman 2009), two-phase behavior of the dissipation term is accommodated, although the assumed physics of Tolman and Chalikov (1996) are different from observed behavior in the experiments by BY05 and YB06, and further do not include the threshold behavior. Alves and Banner (2003) introduced a threshold-like behavior, but the details of the implementation were not entirely consistent with some known features of the measurements (Babanin and van der Westhuysen 2008). Both van der Westhuysen (2007) and Banner and Morison (2010) implemented updated forms of the Alves and Banner (2003) dissipation, incorporating threshold limitations based on observational values. However, these three studies do not apply two-phase wave-breaking dissipation; the cumulative breaking term is omitted, though dissipation similar to that of Komen et al. (1984, hereafter KHH) is used to represent nonbreaking dissipation, that is, swell dissipation. Thus far, the implementation of whitecapping dissipation most consistent with the qualitative features observed in these studies—Banner et al. (2000), Babanin et al. (2001), YB06, and DBYB—was done by Ardhuin et al. (2010). Their formulation is different to that of BY05 and YB06, but they use the same essential features: a cumulative term is included and the same dissipation threshold is used.

Surprisingly, no essential attempts to implement the DBYB input in a two-dimensional (x, y) wave model have been made so far. For example, Ardhuin et al. (2010) utilize the Janssen input (Janssen 1989, 1991), which is developed from the Miles theory (Miles 1957). Such input does not accommodate the air–sea exchange behaviors observed by DBYB and Babanin et al. (2007a) at moderate and extreme weather conditions.

The first implementation of the DBYB wind input and the BY05 and YB06 whitecapping dissipation was done by Tsagareli (2009), and summarized in Tsagareli et al. (2010) and Babanin et al. (2010). This was done within the WAVETIME one-dimensional research model with the exact solution of the nonlinear integral in (1) (van Vledder 2002, 2006). The primary objective of the present paper is to continue the work of Tsagareli et al. (2010) and Babanin et al. (2010) by implementing the new DBYB and BY05 and YB06 source functions in a wave model that can be routinely used to produce two-dimensional forecasts. Documentation of this stepwise development will continue in future manuscripts, most notably with demonstration of practical applications of the model.

The implementation of the BY05 and YB06 dissipation herein also includes an improvement that, as will be shown, allows much simpler calibration, such that it does not depend on wave age (discussed in section 3). The implementation, in addition, is generalized such that the functional dependence of the dissipation on threshold exceedence can, via a parameter selection, be made equivalent to either that used in the other threshold-based dissipation modeling studies (discussed above) or that used by BY05 and YB06. Thus, it is possible to contrast in a concise way the practical impact of fundamental differences between these previously proposed formulations, differences that until now have not been clarified. Section 2 describes the model [Simulating Waves Nearshore (SWAN)], detailing the wind input of DBYB, the dissipation function of BY05 and YB06, and the implemented nonbreaking dissipation sink term, which allows dissipation to continue—albeit much more slowly—after the spectral density has dropped below the breaking threshold. The new physics implementation is calibrated in section 3 using single-point model (duration limited) simulations with older, well-known models used as a baseline, as opposed to standard fetch-limited growth curve analysis. Four possible variants of the new dissipation source function are calibrated in this manner. The observation-consistent dissipation term is then evaluated in section 4 by applying the formula to parametric spectra. The behavior of the model in free simulations is evaluated in section 5, first analyzing the time evolution of the source terms, and then a more traditional analysis, comparing wave growth against empirical expressions. Sections 6 and 7 provide discussion and summary.

2. Model description

The third-generation phase-averaged wave model SWAN (Booij et al. 1999; SWAN Team 2010) is selected as the platform for this study, because, along with WAVEWATCH III (Tolman 1991, 2009), SWAN is one of the two such models under active development for use by the operational U.S. Navy. The governing equation of SWAN is given in (1).

a. Wind-input term

The initial estimate for the wind-input term $S_{\text{in}}(f, \theta)$ is taken from DBYB, with three noteworthy modifications. First, following Tsagareli et al. (2010), a physical constraint is applied to the total stress. Second, the drag coefficient is changed to use a recently proposed formula. Third, spectral saturation is expressed in terms of wavenumber rather than wave frequency.

Here $S_{\text{in}}(f, \theta)$ is calculated from the following equations (from DBYB):

$$S_{\text{in},i}(f,\theta) = B(f,\theta)E(f,\theta), \tag{2}$$

$$B(f,\theta) = \gamma(f,\theta)\sigma\frac{\rho_a}{\rho_w}, \tag{3}$$

$$\gamma(f,\theta) = G\sqrt{B_n(f)}W(f,\theta), \tag{4}$$

$$G = 2.8 - \{1 + \tanh[10\sqrt{B_n(f)}W(f,\theta) - 11]\}, \quad \text{and} \tag{5}$$

$$W(f,\theta) = \left\{\max\left[0, \frac{U}{C}\cos(\theta_{\text{wv}} - \theta_{\text{wn}}) - 1\right]\right\}^2, \tag{6}$$

where $f = \sigma/2\pi$ is the frequency, ρ_a and ρ_w are the densities of air and water, and θ_{wv} and θ_{wn} are the wave and wind directions, respectively. DBYB calibrate this formula based on $U = U_{10}$, the wind speed at 10-m elevation; thus, $U = U_{10}$ is used here. The parameter G is the sheltering coefficient, which accounts for the reduction of atmosphere-to-wave momentum transfer resulting from full airflow separation.

In a slight departure from DBYB, we use the more general form for the spectral saturation dimensionless variable in terms of wavenumber, removing an assumption of deep water,

$$B_n'(f) = A(f)B_n(f) = A(f)(2\pi)^{-1}E(f)k^3C_g, \tag{7}$$

where C_g is the group velocity and k is the wavenumber. Here $A(f)$ is a measure of narrowness of the directional distribution at a frequency (Babanin and Soloviev 1987, 1998), calculated from the directional spectrum normalized by the maximum value of the spectrum at that frequency,

$$E_n(f,\theta) = \frac{E(f,\theta)}{E'(f)}, \tag{8}$$

$$E'(f) = \max[E(f,\theta)], \theta \in [0, 2\pi], \quad \text{and} \tag{9}$$

$$A^{-1}(f) = \int_0^{2\pi} E_n(f,\theta)\, d\theta. \tag{10}$$

A constraint on the computed normal stress is applied, which we refer to as a ''physical constraint,'' because it is a constraint on the model physics, specifically S_{in}. The physical constraint is that the normal stress may not exceed the total stress less the viscous (tangential stress) and any other stress that is not estimated,[1]

$$\tau_{\text{norm}} = \tau_{\text{tot}} - \tau_\nu - \tau_{\text{unknown}}. \tag{11}$$

Thus, the implemented constraint is $\tau_{\text{norm}} \leq \tau_{\text{tot}} - \tau_\nu$ and we only modify the wind-input term if $\tau_{\text{norm}} > \tau_{\text{tot}} - \tau_\nu$. This is done by checking the initial estimate $S_{\text{in},i}(f, \theta)$ against the maximum possible normal stress level from (11). For purposes of this check, the nondirectional form of S_{in} is used, $S_{\text{in}}(f) = \int_0^{2\pi} S_{\text{in}}(f,\theta)\, d\theta$, following Tsagareli et al. (2010). The normal stress calculation is

$$\tau_{\text{norm}} = \rho_w g \int_{f_1}^{10\,\text{Hz}} \frac{S_{\text{in}}(f)}{C} df, \tag{12}$$

where C is the phase velocity and f_1 is the lowest modeled frequency, usually around 0.04 Hz. The high-frequency tail of the spectrum is important to stress calculations, so a diagnostic tail is added to $S_{\text{in}}(f)$. Specifically, $S_{\text{in}}(f)$ is extended to $f = 10$ Hz using an approximation for the spectral slope $S_{\text{in}}(f) \propto f^{-2}$ [at the high-frequency limit, and for $E(f) \propto f^{-5}$, the DBYB input has this slope exactly]. The total and viscous stresses are calculated from

$$\tau_{\text{tot}} = U_*^2\rho_a = C_D U_{10}^2 \rho_a \quad \text{and} \tag{13}$$

$$\tau_\nu = C_\nu U_{10}^2 \rho_a, \tag{14}$$

[1] Values of $\tau_{\text{norm}}/\tau_{\text{tot}} < 60\%$ are reported in the literature as being typical (Snyder et al. 1981; Hsu et al. 1981; Hsu et al. 1982). Taken with the fact that our estimated viscous stress is generally small, this suggests that these nonestimated stresses may be significant, consistent with our presentation here: that $\tau_{\text{tot}} - \tau_\nu$ is really the upper limit on the normal stress and may be 30%–50% higher than the actual normal stress.

where C_v is based on the data of Banner and Peirson (1998), as applied by Tsagareli et al. (2010),

$$C_v = \max(-5 \times 10^{-5} U_{10} + 1.1 \times 10^{-3}, 0). \quad (15)$$

In this study, the drag coefficient C_D is taken from Hwang (2011),

$$C_D = 1 \times 10^{-4}(-0.016U_{10}^2 + 0.967U_{10} + 8.058). \quad (16)$$

This formula is a fitting to the datasets of Powell et al. (2003) and Jarosz et al. (2007) and provides saturation of the sea drag at wind speeds in excess of 30 m s^{-1}, and even a decrease of the drag at very strong winds. The behavior is strictly empirical, though it has been speculated (Powell et al. 2003) that one cause of the reduction of total stress could be full airflow separation, as is explicitly included in our wave-supported stress implementation (5). Because there is no upper limit on the wind speed that a user might provide to SWAN, it is necessary to modify the Hwang formula to prevent the drag coefficient from dropping to zero at extreme wind speeds, where reliable measurements do not exist to provide guidance. We use the simplest possible modification, applied at the U_{10}, where $\partial U_*/\partial U_{10} = 0$ in Eq. (16): $U_* = 2.026$ m s^{-1} for $U_{10} \geq 50.33$ m s^{-1}. In the cases presented herein, which are not for hurricane wind speeds, this modified Hwang expression yields drag coefficients that do not substantially deviate from those obtained with the default formula of SWAN, which is a modified form of Wu (1982; see section 6 of WAMDIG 1988), though it does necessitate a slightly different calibration of the dissipation coefficients a_1 and a_2 (see section 3 here). This topic of drag coefficient will be treated in greater detail in a second manuscript, which does include hurricane wind speeds.

For the case of $\tau_{\text{norm}} > \tau_{\text{tot}} - \tau_v$, it is necessary to reduce the S_{in} to satisfy our constraint. We use the reduction $S_{\text{in},r}(f) = L_r(f)S_{\text{in},i}(f)$, where

$$L_r(f) = \min[1, P(f)] \quad \text{and} \quad (17)$$

$$P(f) = \exp\left[\left(1 - \frac{U}{C}\right)R_\tau\right]. \quad (18)$$

This serves the same purpose as a comparable reduction applied by Tsagareli et al. (2010). Here, the reduction strength is controlled by parameter R_τ, which is determined via iteration such that $\tau_{\text{norm}} = \tau_{\text{tot}} - \tau_v$. The form of the Eq. (18) is designed to disproportionately reduce the stress contribution from higher frequencies. This is based on a practical consideration—early experiments using a model with the DBYB input formulation without any reduction revealed a tendency to overpredict high-frequency energy. Also, as discussed in Tsagareli (2009) and Tsagareli et al. (2010), essential corrections to the spectral peak area are to be avoided because this is where the wind input was actually measured in DBYB. Thus, the implemented reduction serves a dual purpose of enforcing a physical constraint (11), while also reducing the overestimation of energy at high frequencies. An unintended consequence of the design is that a greater portion of the reduction to $S_{\text{in}}(f)$ is applied in the diagnostic tail region, where $S_{\text{in}}(f)$ has no influence on model calculations.

An example of the implemented DBYB source function, before and after application of $L_r(f)$, is shown in Fig. 1. The default $S_{\text{in}}(f)$ used by the SWAN model, based on the work of Snyder et al. (1981) and KHH, is also shown. The directional spectrum used as input to the two formulas is identical and is taken from application of the new model in an unlimited fetch scenario (section 3) for 12 h with $U_{10} = 12\,\text{m}\,\text{s}^{-2}$, which is also the wind speed provided to the two formulas here. The most important feature of the DBYB $S_{\text{in}}(f)$ is that, because of the dependence $((U/C) - 1)^2$ rather than $((U/C) - 1)$ as of the Snyder–Komen model, it tends to be weaker close to the peak ($<2f_p$ in the example shown) and stronger at higher frequencies ($>2.5f_p$ in the example shown). As will be shown later, this has a profound implication on the required behavior of the dissipation term. As expected, the impact of the reduction via application of $L_r(f)$ is primarily in the diagnostic tail (for SWAN, this is typically applied after 1.0 Hz), but there is still a substantial reduction in the prognostic region. The contribution of each frequency bin to the total stress is plotted in the lower panel. The contribution is nearly constant in the saturation region, with the slight deviation being due to the "−1" in (6), such that it is, in fact, constant at the high-frequency limit.

b. Whitecapping dissipation

The observation-consistent whitecapping term $S_{\text{ds}}(f, \theta)$ used in this study is based on that proposed by BY05 and YB06 having two key features. The first is that waves do not break unless the spectral density at that frequency exceeds a threshold spectral density calculated from the spectral saturation spectrum (see Banner et al. 2000; Babanin et al. (2001, and section 1). The saturation spectrum is defined by Phillips (1984) as $B = g^{-1/2}k^{9/2}N(\mathbf{k})$. In terms of frequency spectra, the threshold spectral density is calculated as

$$E_T(f) = \frac{2\pi B_{\text{nt}}}{A(f)C_g k^3}, \quad (19)$$

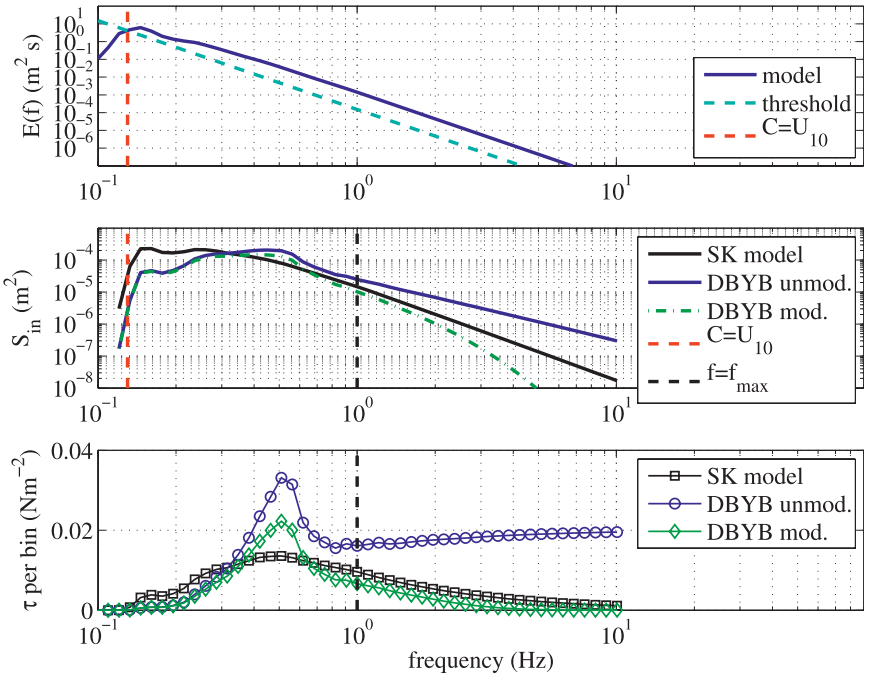

FIG. 1. Source function calculations for $U_{10} = 12\,\mathrm{m\,s^{-1}}$. (top) Energy density spectrum used for calculations (omnidirectional form, whereas calculations are made on directional spectrum). Frequency corresponding to $C = U_{10}$ is indicated, as is wave-breaking threshold as described in section 2b. (middle) $S_{\mathrm{in}}(f)$. Snyder et al. (1981)/Komen et al (1984) model (SWAN default; solid black line), DBYB prior to application of $L(f)$ (blue line). DBYB after application of $L(f)$, that is, $\tau_w = \tau_{w,\mathrm{lim}}$ (green line). (bottom) Contribution of each frequency bin to the total stress (frequency grid is logarithmic). The separation between the prognostic spectrum and diagnostic tail for a typical SWAN application (and all applications presented herein; black dashed line).

where B_{nt} is an empirical constant following the investigation of wave-breaking probabilities by Babanin et al. (2007b), $\sqrt{B_{\mathrm{nt}}} = 0.035$. Once this threshold is exceeded, the dissipation depends critically upon the level of exceedence, $\Delta(f) = E(f) - E_T(f)$. An example threshold spectrum $E_T(f)$ is shown in the top panel of Fig. 1.

The second key feature of the whitecapping term is that it is two phase, because it has been hypothesized to be separable into two distinct mechanisms (YB06); thus, there are two separate dissipation terms,

$$S_{\mathrm{ds}}(f,\theta) = T_1(f,\theta) + T_2(f,\theta). \tag{20}$$

The first dissipation mechanism is the inherent breaking component T_1, which accounts for breaking resulting from instabilities of waves at that frequency,

$$T_1(f,\theta) = a_1 A(f) f \left[\frac{\Delta(f)}{\tilde{E}(f)}\right]^L E(f,\theta). \tag{21}$$

The second breaking component T_2 accounts for the dissipation of waves induced by the breaking of longer waves, for example, via turbulence created by such breaking events. It is not expected that short breaking waves will destabilize longer waves. Thus, the calculation is based on an integration of the normalized threshold exceedence from the first prognostic frequency up to the frequency in question. Thus, T_2 is a cumulative term, not local in frequency–wavenumber space,

$$T_2(f,\theta) = a_2 \left[\int_{f_1}^{f} A(f') \left[\frac{\Delta(f')}{\tilde{E}(f')}\right]^M df'\right] E(f,\theta). \tag{22}$$

Here a_1 and a_2 are coefficients for calibration, discussed in detail below. The exceedence levels $\Delta(f)$ are normalized by a generic spectral density $\tilde{E}(f)$, which can be either $E(f)$ or $E_T(f)$. With normalization by $E_T(f)$, the equations become similar to that used by Ardhuin et al. (2008), which have since been extended to directional form by Ardhuin et al. (2010). With normalization by $E(f)$, the equation becomes similar to that of BY05 and YB06, Tsagareli (2009), and Babanin et al. (2010).[2]

[2] It is similar, but not identical, because in those papers, the normalization by $E(f)$ is outside the integral of T_2. The practical impact of this difference will be discussed in section 3.

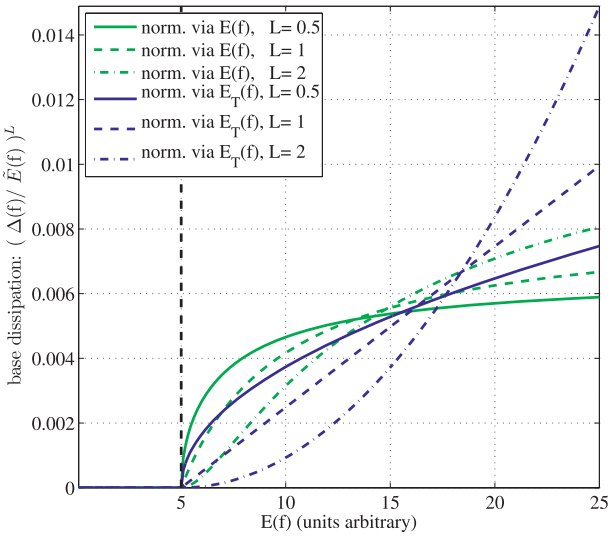

FIG. 2. Qualitative demonstration of expected impact of the choice of normalization variable and choice of power coefficient L. The vertical axis shows a dissipation quantity that has been normalized by the total area under each curve in the region plotted to aid viewing and roughly approximate the effect of calibration. Here, only one frequency is shown, and the E_T at this frequency is 5 (units are unimportant here), so dissipation is zero for $E < 5$.

The normalization allows us to use the power coefficients L and M, which can control how strongly the dissipation term reacts to threshold exceedence. Figure 2 illustrates the expected impact of the choice of $\tilde{E}(f) = E_T(f)$ versus $E(f)$ and choice of coefficients L and M. It is clear that using a power coefficient greater than unity in combination with the Ardhuin form $\tilde{E}(f) = E_T(f)$ implies that the dissipation will become very large as the exceedence increases, whereas the form $\tilde{E}(f) = E(f)$ applied by BY05 and YB06 demonstrates less sensitivity. This is because $[\Delta(f)/E(f)]^L$ is always less than unity, whereas for $L > 1$, $[\Delta(f)/E_T(f)]^L$ can become large quickly as the exceedence $\Delta(f)$ is increased.

The directional narrowness parameter A is set to unity in all dissipation calculations. This parameter was introduced by BY05 to provide consistency with Banner et al. (2002), but more recent analysis by Babanin (2009, see discussion of Fig. 5.28) suggests that whenever the cumulative term is included, the parameter may be unnecessary. Further, it may have a negative impact on accuracy at the higher frequencies. This is discussed in more detail in section 6.

c. *Nonbreaking dissipation (swell dissipation)*

The new S_{ds} formulation represents the rapid dissipation from breaking waves. In a decaying wind-sea situation, once the spectral density falls below the breaking threshold E_T, it can no longer be dissipated via our S_{ds} formula. It is therefore necessary to also represent the relatively slow dissipation of nonbreaking waves, as would occur in this situation. For this separate sink term, we adopt the method of Ardhuin et al. (2009). This method uses one of two calculations, depending on whether the atmospheric boundary layer at the sea surface is either turbulent or laminar. This is based on Reynolds number $\mathrm{Re} = (4u_{\mathrm{sig},a}a_{\mathrm{orb}}/\nu_a)$, where ν_a is the viscosity of the air, a_{orb} is half the significant wave height, calculated for the total energy (i.e., sea surface variance) as $a_{\mathrm{orb}} = 2\sqrt{E_{\mathrm{tot}}}$, and $u_{\mathrm{sig},a}$ is the significant orbital velocity amplitude at the surface, related to the rms orbital velocity amplitude and rms orbital velocity as $u_{\mathrm{sig},a} = \sqrt{2}u_{\mathrm{rms},a} = 2u_{\mathrm{rms}}$.

For $\mathrm{Re} > \mathrm{Re}_{\mathrm{cr}}$,

$$S_{\mathrm{swell}}(f,\theta) = \frac{16}{g}\frac{\rho_a}{\rho_w} f_e \sigma^2 u_{\mathrm{sig},a} E(f,\theta). \tag{23}$$

For $\mathrm{Re} \le \mathrm{Re}_{\mathrm{cr}}$,

$$S_{\mathrm{swell}}(f,\theta) = 2\frac{\rho_a}{\rho_w} C_{\mathrm{ds},\nu} k \sqrt{2\nu_a \sigma} E(f,\theta). \tag{24}$$

In simulations herein, we use $\mathrm{Re}_{\mathrm{cr}} = 2 \times 10^5$, $C_{\mathrm{ds},\nu} = 1.2$, and f_e of values up to 0.013, based on Ardhuin et al. (2010). However, whereas those authors allow f_e to vary with wind speed and $\mathrm{Re}_{\mathrm{cr}}$ to vary with wave height, we specify each as constant for a given simulation.

3. Preliminary model calibration

The wind-input source function $S_{\mathrm{in}(f)}$ as described in section 2a is not calibrated because it is preferred that the implemented source function should not deviate from the original observation-consistent form given by DBYB within the frequency range $f < 2f_p$, where measurements were made. The observation-consistent $S_{\mathrm{ds}}(f)$ formulation, on the other hand, has four free parameters to be set (a_1, a_2, L, and M), plus the selection of $\tilde{E}(f) = E(f)$ versus $\tilde{E}(f) = E_T(f)$. The first two parameters are objectively determined via calibration in this section. The latter three choices are somewhat more subjective, so we present four possible variants of the model based on these choices [L, M, and $\tilde{E}(f)$], and evaluate their merits. All calibrations are performed within the SWAN model.

Babanin et al. (2010) adopt $L = M = 1$ and $\tilde{E}(f) = E(f)$. The choice of $L = 1$ is based on observational evidence, namely, that T_1 should have linear dependence on $\Delta(f)$ (YB06). Herein, we denote this form as DL1M1, where "D" indicates the concave down form of $\tilde{E}(f) = E(f)$ in Fig. 2. The $\tilde{E}(f) = E_T(f)$ form in Fig. 2

is concave up for all values of $L > 1$, so this is denoted with "U." It is readily apparent from Fig. 2 that the $\tilde{E}(f) = E_T(f)$ model is much more sensitive to L and M than the $\tilde{E}(f) = E(f)$ model. Thus, we include three variants of the former in comparisons herein, namely, UL2M2, UL1M4, and UL4M4, and only one of the latter, DL1M1. For brevity, these four variants are referred to below as the "new models," though they are all based on a single implementation of the new physics in the SWAN code.

The traditional method of determining dissipation term calibration coefficients equivalent to (a_1, a_2) is by matching to fetch-limited growth curves. For example, Tolman and Chalikov (1996) calibrated five free parameters comparable to our a_1, a_2, L, and M using the Kahma and Calkoen (1992) empirical expressions. We diverge from this tradition in two ways. First, we use duration-limited wave growth rather than fetch-limited wave growth. Only a single grid point is modeled, zeroing propagation velocities, in effect representing the model domain as an infinitely deep and wide ocean with no spatial gradients, $\mathbf{\nabla} \cdot \mathbf{c}N = 0$. This simple design has an obvious computational advantage but also makes it less likely that the results will be contaminated by numerical error or spurious swell components traveling at large angles to the wind.[3] The second break from tradition is that we do not use empirical growth curves. Rather, we compare the new physics implementation with two models that have already been proven as robust and skillful, at least in the context of wind-sea-dominated conditions. If results from a new model are bounded by these two thoroughly tested models, then that model can be considered preliminarily calibrated, and this further constitutes an indirect check against historical observations under nonidealized conditions. Further, results can be interpreted in the context of the well-known behavior of these models. For these two models, we use the KHH form as implemented in SWAN, using 1) the dependence on relative wavenumber as favored by KHH, $n = 1$, and 2) an alternate dependence, as used by the author in Rogers et al. (2003) and frequently used since then, $n = 2$, where the KHH is $S_{ds}(f) \propto (k/k_m)^n$, and k_m is the mean wavenumber. The first KHH form is the default setting in SWAN. The second setting corrects a well-known systematic tendency by SWAN (with the first default setting) to underpredict the mean wave period; for further detail, see Rogers et al. (2003). A time step of 30 s is used in all single-point model simulations. The discrete interaction approximation (DIA) method (Hasselmann et al. 1985; SWAN 2010) of computing S_{nl} is employed; implications of this are discussed in section 6. Testing for realistic, two-dimensional applications is also essential; this has been done and will be reported separately.

Figure 3 illustrates the calibration process. [For mathematical definitions of H_{m0} and T_{m01} and frequency narrowness, the reader is referred to SWAN (2010).] The case of $U_{10} = 12$ m s^{-1} is shown; other wind speeds show comparable results, because the models scale with U_* with only minor variations. Note, however, that because the KHH models use the modified Wu (1982) C_d formulation (WAMDIG 1988), they scale differently from the new models, most noticeably at high wind speeds. The nonbreaking dissipation term $S_{swell}(\sigma, \theta)$ is not included in this calibration; this term acts on the entire spectrum even for wind-sea-dominated cases, so including it would introduce additional free parameters into the calibration process. For this reason in particular, the calibration herein should be regarded as preliminary, with the final calibration to be obtained later using comparison to observations in major ocean basins with both wind sea and swell. Because $S_{swell}(\sigma, \theta)$ is omitted, we calibrate the (a_1, a_2) coefficients of each model to match the higher wave height of the two baseline models, KHH's $n = 2$. The wave height comparison indicates one possible problem: energy growth during the young wave age stage of the simulation, with energy there exceeding that of either KHH model. This is attributable to the dependence of the DBYB wind input on $[(U/C) - 1]^2$ and $B_n'(\sigma)$, and is worst with the DL1M1 model, while it is not noticeable with the UL4M4 model. The T_{m01}, T_p, and frequency narrowness comparisons mostly show good agreement, though it is noted that the DL1M1 model T_{m01} tracks closely the KHH $n = 1$ model, so we can anticipate that this model, in real applications, will tend to underpredict mean spectral period like the KHH $n = 1$ model. Comparison of the one-dimensional spectra (not shown) indicates a tendency of these two models to overpredict high-frequency energy.

These two coefficients (a_1, a_2) can be adjusted independently, and because a relatively strong T_2 will generally increase the dissipation of higher frequencies, we find that there is some sensitivity of mean spectral period T_{m01} to the relative magnitude a_1/a_2. Thus, it may be possible to calibrate the T_{m01} growth curves of the models in this fashion. However, we do not take this approach. Rather, we calibrate the a_1/a_2 ratio of each model to yield a frequency-integrated T_1/T_2 ratio that is consistent with our understanding of dissipation in the real ocean, namely, that for fully developed waves the

[3] This is a common problem in idealized fetch-limited simulations using any model without a strong swell dissipation mechanism. Nonlinear interactions in the model create swell components that are opposing the wind direction, that is, traveling toward the zero-fetch location, and the model predicts nonzero energy at this location.

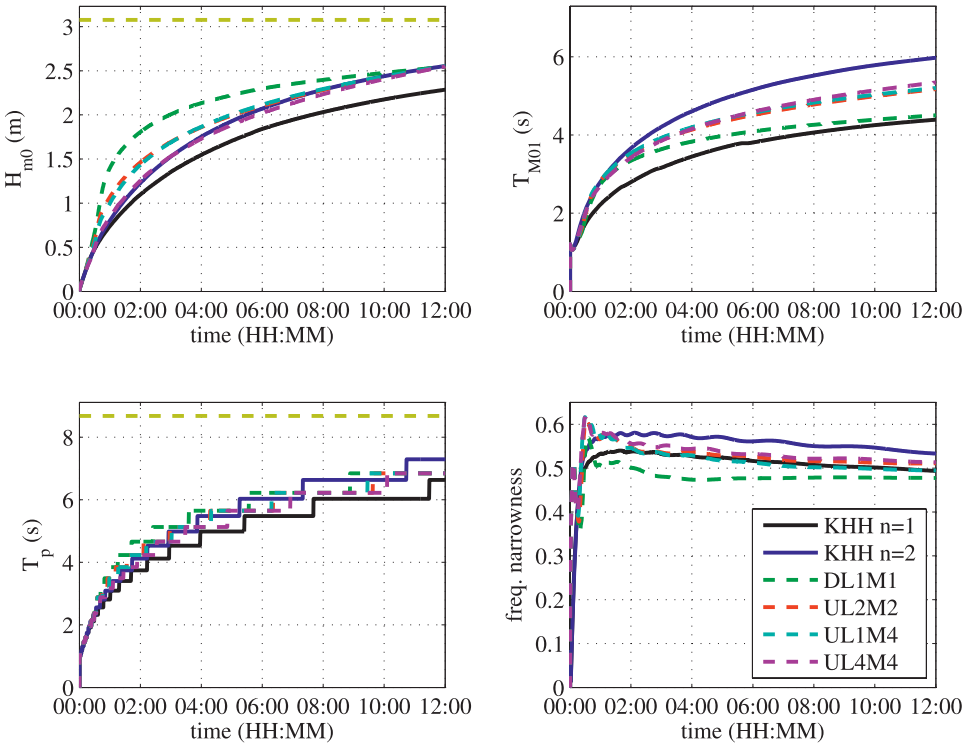

FIG. 3. Calibration using single-gridpoint simulations. Calculations are for $U_{10} = 12$ m s^{-1} and a 12-h duration is shown. Pierson and Moskowitz (1964) limit (yellow dashed line), determined as by KHH, Booij et al. (1999), van der Westhuysen et al. (2007), and others, with U^* scaling $f^*_{PM} = f_{PM}u_*/g = 5.6 \times 10^{-3}$; $E^*_{PM} = E_{PM}g^2/u_*^4 = 1.1 \times 10^3$, with C_d from Wu (1982), thus implying some deviation from the value of PM, which scales instead with $U_{19.5}$. Frequency narrowness is dimensionless from integration of the one-dimensional spectrum, as defined by Battjes and van Vledder (1984) and SWAN (2010).

dissipation should be dominated by the induced term T_2 (Babanin et al. 2010). This also implies a certain level of consistency between the models, which aids in interpreting later results. The terms ''fully developed'' and ''dominated'' are qualitative in nature; we semiarbitrarily calibrate (a_1, a_2) such that the contribution of T_2 after 12 h in the $U_{10} = 12$ m s^{-1} simulation is 75%–80% of the total dissipation. This constitutes a physical constraint, though it is applied in the calibration process, as opposed to a constraint that is enforced during every execution of the model, as with the constraint on total stress. Table 1 gives the calibration coefficients for each of the four models. Figure 4 shows the UL1M4 results for the first 1.5 h at this wind speed. From the study of J.-F. Filipot (2010, personal communication), which utilizes the dataset of Manasseh et al. (2006), we expect that the transition at $3f_p$ from majority T_1 to majority T_2 dissipation (i.e., the 50/50 crossover point) should happen either at or before the wave age values correspond to the Manasseh et al. study (see their Table 1). Specifically, we expect the crossover to occur at inverse wave ages U_{10}/C_p of 3.5 or larger (i.e., earlier). The model does conform to this expectation, with the crossover occurring quite early, during the first 10 min of the simulation.

Babanin et al. (2010) determined (a_1, a_2) such that the model ratio of integrated dissipation to integrated input $R = D_{tot}/I_{tot} = \int S_{ds}(f)\,df / \int S_{in}(f)\,df$ matched a predetermined function based on observations (Donelan 1998; see section 5a below). An unusual feature of their dissipation is that the (a_1, a_2) coefficients were a function of wave age, varying by a few orders of magnitude over the typical wave age range. In our own simulations with the original BY05 and YB06 form of the dissipation, we also found that (a_1, a_2) must vary with wave age in order to achieve satisfactory results, and initially

TABLE 1. Coefficients used for each of the four models. $\tilde{E}$ is the normalization variable, $\tilde{E}(f) = E(f)$ or $\tilde{E}(f) = E_T(f)$.

$\tilde{E}(f)$	L	M	a_1	a_2
$E(f)$	1	1	2.0×10^{-4}	1.6×10^{-3}
$E_T(f)$	2	2	8.8×10^{-6}	1.1×10^{-4}
$E_T(f)$	1	4	5.7×10^{-5}	3.2×10^{-6}
$E_T(f)$	4	4	5.7×10^{-7}	8.0×10^{-6}

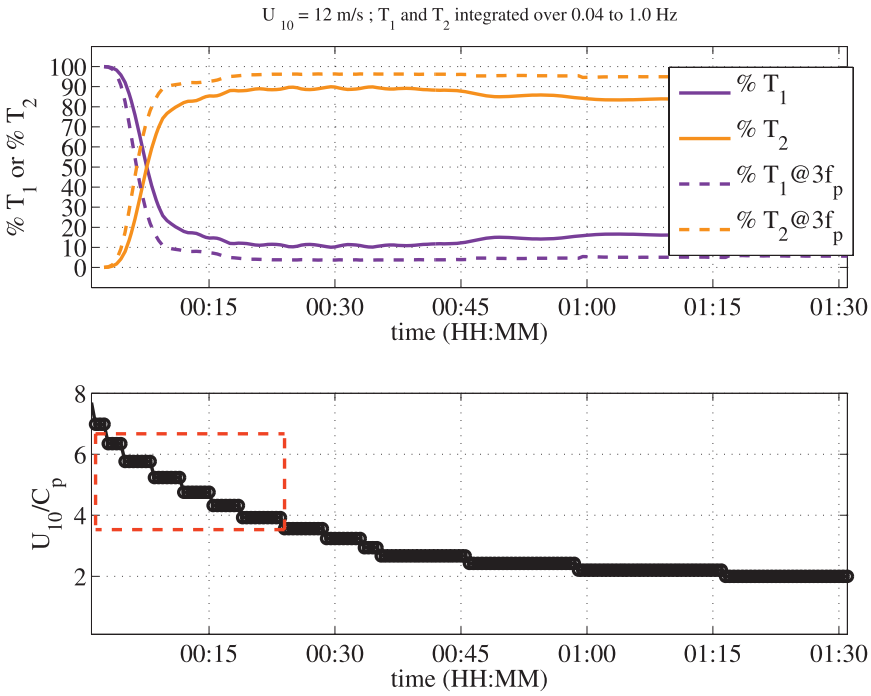

FIG. 4. (top) Contribution of T_1 vs T_2 to the total dissipation for the UL1M4 $U_{10} = 12$ m s^{-1} simulation. The integrated T_1 and T_2 values (solid lines) and the values at $3f_p$ (dashed lines). (bottom) Inverse wave age for the same simulation. Wave age and time period corresponding to the Manasseh et al. (2006) study are indicated (dashed-line box).

developed complicated lookup tables to be used by the model to determine the coefficients during run time. However, by modifying the $T_1(f)$ calculation such that the normalization occurs *within* the integral as shown in (22), we find that a single pair of coefficients can be used, and the lookup table procedure becomes obsolete.

Summarizing the calibration procedure, we find for each of four models two coefficients (a_1, a_2) that yield the best match of total energy in idealized duration-limited simulations to two preexisting models, one being the default physics of SWAN (version 40.72). The relative size of a_1 versus a_2 is set to achieve a desired ratio of T_1 versus T_2 at large wave age values at moderate wind speeds, thereby ensuring some degree of consistency between models with regard to this ratio. No calibration is performed for mean spectral period or any other bulk parameter associated with spectral distribution of energy.

4. Dissipation model on parametric spectra

In this section, to further examine the frequency-dependent characteristics of the calibrated dissipation model, we analyze calculations with the new observation-consistent dissipation term on parametric spectra. Whereas in other sections the time evolution of spectra is modeled, computations here are performed outside the wave model, and interactions with other source terms are not considered.

a. Description of composite parametric spectra

Because the directional dependence of the new dissipation function (20) only exists via the multiplication by the directional spectrum, that is, $K_{ds}(f) = S_{ds}(f,\theta)/E(f,\theta) = S_{ds}(f)/E(f)$, the computations can be performed on omnidirectional parametric spectra. There is considerable evidence for wave frequency spectra exhibiting two subranges: f^{-4} dependence closer to spectra peak and f^{-5} dependence at higher frequency (Forristall 1981; Ewans and Kibblewhite 1990; Hwang and Wang 2001). The representative parametric spectra is modeled as a composite function of both slopes separated by a transition frequency, which is

$$E(f) = \begin{cases} E_{\mathrm{Don}}(f), & f \le f_{\mathrm{tr}} \\ E_{\mathrm{Don}}(f_{\mathrm{tr}})\left(\dfrac{f_{\mathrm{tr}}}{f}\right)^{-5}, & f > f_{\mathrm{tr}} \end{cases}. \qquad (25)$$

Here, our composite spectra has $f_{\mathrm{tr}} = 3f_p$ based on references cited above.

The $E_{\mathrm{Don}}(f)$ is the spectral model proposed by Donelan et al. (1985),

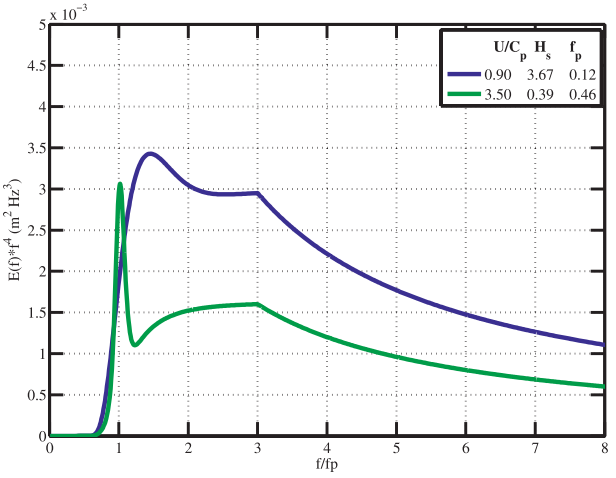

FIG. 5. The composite parametric spectra described in the text. All models have the same wave height and peak period. Vertical axis: $(f)f^4$. Horizontal axis: f/f_p.

$$E_{\mathrm{Don}}(f) = \frac{\alpha_{\mathrm{Don}} g^2}{(2\pi)^4 f_p} f^{-4} \times \exp\left[-\left(\frac{f_p}{f}\right)^4\right]^{\gamma_{\mathrm{Don}}^{\exp\left[-0.5\left(\frac{f-f_p}{\sigma_{\mathrm{Don}} f_p}\right)^2\right]}}, \quad (26)$$

where the coefficients α_{Don}, γ_{Don}, and σ_{Don} are the equilibrium range (rear face) parameter, the peak enhancement factor, and the peak width parameter, respectively, and can be determined based on inverse wave age U_{10}/C_p shown in Young (1999). This is very similar to the "Combi spectrum" as given by Tsagareli (2009) and Babanin et al. (2010), though those authors use $f_{\mathrm{tr}} = 2.5g/\pi U_{10}$, following Kahma and Calkoen (1992). The composite parametric spectra are illustrated in Fig. 5 for wind speed $U_{10} = 12$ m s^{-1} and U_{10}/C_p of 0.9 and 3.5 corresponding to, respectively, fully developed and young seas.

b. Spectral dissipation

In the point model simulations, the spectral distribution is allowed to evolve freely, so each of the four models produce different spectral shapes: this is evident from the different peak period, mean spectral period, and frequency narrowness in Fig. 3. However, it is useful to compare computations of dissipation term on identical spectra to contrast the unique behavior of each model. The four new dissipation functions, applied to the composite spectral model for fully developed and young seas, are shown in Fig. 6. The simulation for a fully developed sea (Fig. 6a) reveals remarkable differences between the dissipation functions. In particular, the $\tilde{E}(f) = E(f)$ dissipation model DL1M1 predicts that most dissipation is in the region of $f < 2f_{\mathrm{p}}$, whereas the $\tilde{E}(f) = E_T(f)$ model UL4M4 predicts that most dissipation will occur in the region of $f > 2f_{\mathrm{p}}$. We further point out that the dominant wave breaking is zero or near zero for the fully developed spectrum. This behavior is consistent with what occurs in the real ocean (YB06).

For a young sea (Fig. 6c), all four functions show most dissipation occurring at or near spectral peak. Of the four models, the UL4M4 model demonstrates a significant bimodal distribution in frequency space, with dissipation peaking near the spectral peak and near $3f_p$. Recall that all models were calibrated in section 3 such that the frequency-integrated T_1 versus T_2 ratio is roughly consistent between them at the quasi-equilibrium state; the ratios of T_1 and T_2 seen in Figs. 6b,d reflect this. This is qualitatively similar to the maximum breaking rates reported by Babanin et al. (2007b), which showed an initial strong increase with frequency, then a leveling off or slight decrease. However, there are limits to such comparisons, because dissipation rate is dependent on not only breaking rate but also breaking intensity.

The behavior of the models clearly demonstrate that it would be a mistake to conflate T_1 with low-frequency dissipation or T_2 with high-frequency dissipation: the two modes coexist for all frequencies above the peak.

5. Model behavior in free simulations

In this section, we utilize the same duration-limited simulations as described in section 3. Simulations are "free" insofar as spectra are time evolving and not prescribed (cf. section 4 above). The behaviors of the new observation-consistent input and dissipation formulas are analyzed here, first by evaluating the time evolution of the integrated source terms, and then comparing duration-limited growth curves against empirical growth curves.

a. Time evolution of source terms

Frequency-integrated source terms from the point model simulations are shown in Fig. 7. As expected, the DBYB wind term is stronger for younger waves, being calculated from $((U/C) - 1)^2$ rather than $((U/C) - 1)^1$, as with the KHH input term. After the period of initial growth, all of the new models show a slow weakening of the wind-input term with a slow strengthening of the dissipation term. The former is due to the effect of the downshifting of the spectrum on wave celerity C. The integral of the nonlinear terms is expected near zero, deviating some because the maximum frequency for integration is only 1.0 Hz.[4] The two models with a tendency

[4] Ideally, the computation should be performed using an accurate nonlinear solver, for example, as used by Tsagareli et al. (2010), and extended into high frequencies (e.g., 10 Hz).

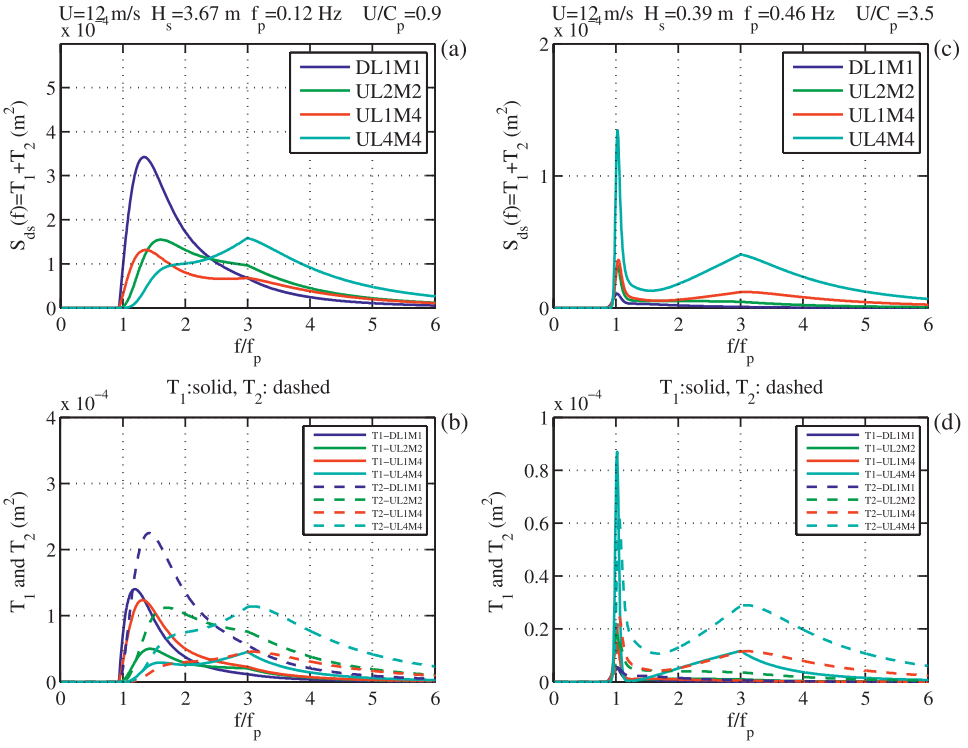

FIG. 6. (a),(c) $S_{ds}(f)$ vs f/f_p. (b),(d) $T_1(f)$ and $T_2(f)$ vs f/f_p. (a),(b) Fully developed wave conditions $U_{10}/C_p = 0.9$. (c),(d) Young wave conditions $U_{10}/C_p = 3.5$. The models shown are the same as those in Fig. 3. Computations are on the parametric spectrum with transition at $f_{tr} \sim 3f_p$, and are for the case of $U_{10} = 12$ m s^{-1}.

to overpredict high-frequency energy, DL1M1 and KHH's $n = 1$, both show especially strong negative values for $\int S_{nl}(f)\,df$; apparently the nonlinear term is partially compensating for weak S_{ds} in the higher frequencies by transferring energy from the high-frequency range to the diagnostic tail. All of the new models show similar values for $D_{tot} = \int S_{ds}(f)\,df$ for large wave age values, but during the initial stages of strong growth, the D_{tot} of the $\tilde{E}(f) = E_T(f)$ models are larger than that of the KHH $n = 2$ model (compensating the strong input from the DBYB S_{in}), whereas that of the $\tilde{E}(f) = E(f)$ model (green dashed line) is quite weak at this stage. The two $M = 4$ models show some oscillation of S_{ds} at these early stages; this is apparently associated with high-frequency energy.

The lower right panel of Fig. 7 shows the ratio between dissipation and input, $R = D_{tot}/I_{tot} = \int S_{ds}(f)\,df / \int S_{in}(f)\,df$. According to Donelan (1998) (see also Fig. 4 of Babanin et al. 2010), this ratio should diminish from 0.85 at $U_{10}/C_p \sim 5.5$ to 0.97 at $1.5 < U_{10}/C_p < 4.5$. Unlike Babanin et al. (2010), we do not enforce this ratio as a physical constraint but allow it to develop freely. (This is discussed further in section 6.) All of the new models predict ratios lower than that suggested by Donelan (1998). By 2 h into the simulation, all models except for DL1M1 consistently show $R \approx 0.7$, which is still lower than the Donelan (1998) value of $R = 0.97$. Increasing the frequency range of computations increases the ratio only modestly, with computations to 10.0 Hz (not shown), $R = 0.92$ after 12 h with the UL4M4 model, compared to $R = 0.87$ with computations to 1.0 Hz (shown).

b. *Energy growth versus empirical expressions*

Traditionally, empirical growth curves, such as those of Kahma and Calkoen (1992) nondimensionalized and plotted on logarithmic scaling, are used to calibrate wave models (e.g., Tolman and Chalikov 1996; van der Westhuysen et al. 2007). Such growth curves were not considered in our calibration, but it is worthwhile to compare to such expressions post facto, as we do now. Duration- rather than fetch-limited comparisons are made, for reasons explained in section 3. The comparison is shown in Fig. 8. Here, the nondimensionalized time is $\zeta = gt/U_{10}$ and the nondimensionalized energy is $\varepsilon = (Eg^2/U_{10}^4)$, where E is the total variance or energy.

As in Fig. 3, we include the KHH $n = 1$ and KHH $n = 2$ models for reference. However, rather than showing

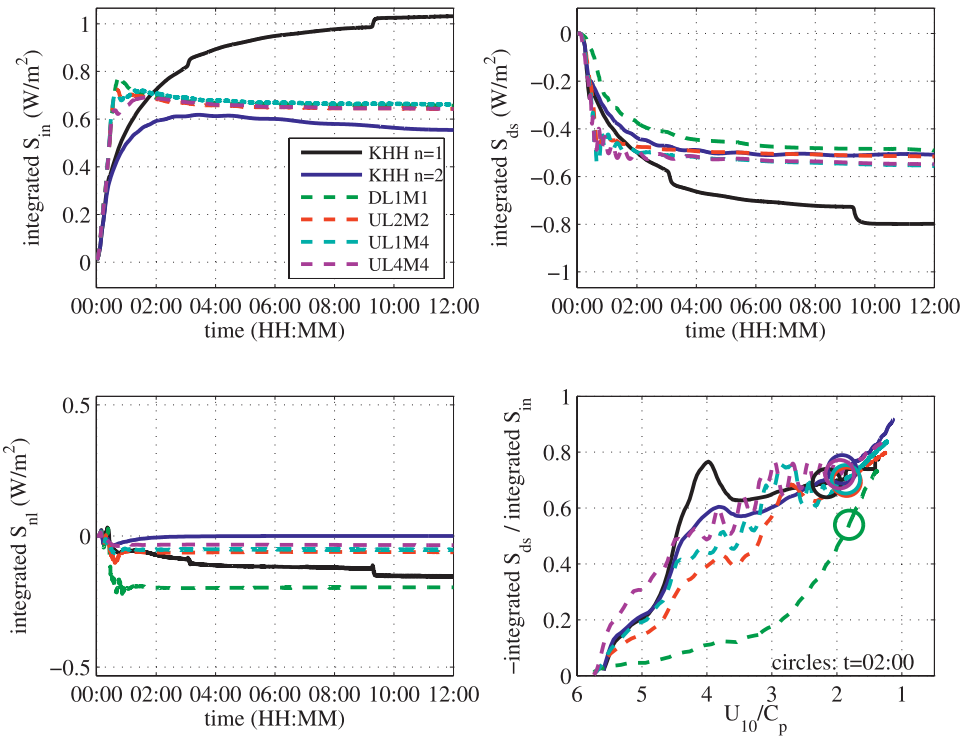

FIG. 7. Frequency-integrated source terms. Models shown are the same as those shown in Fig. 3. (bottom right) The ratio between dissipation and input vs inverse wave age is shown, with circles indicating the points 2 h into each simulation. The frequency range for the integration is 0.042–1.0 Hz.

the same new models as in Fig. 3, we use this opportunity to quantify the sensitivity to the primary coefficient controlling the strength of nonbreaking dissipation. We select a single model (UL4M4) and vary the parameter f_e. Recall that $f_e = 0$ in Fig. 3; the other two values shown here are $f_e = 0.006$ and $f_e = 0.011$, based on the recommendation by Ardhuin et al. (2009, 2010) that $0.004 < f_e < 0.013$ is a reasonable range of values in the large ocean basins. The UL4M4 model is selected for this because, based on comparison in Fig. 3 of the four new models, it is the one expected to have the fewest problems with overprediction of high-frequency energy in subsequent, more realistic simulations. All numerical model growth curves are created using simulations with $U_{10} = 12$ m s^{-1}.

The four empirical growth curves included are as follows:

1) A linear fit to the tabulated data of Stewart (1961), $\varepsilon = 8 \times 10^{-9}\zeta^{1.2}$ within the range $10 \times 10^3 < \zeta < 22.0 \times 10^3$.
2) The Sanders (1976) growth curve, as presented by Young (1999, e.g., his Fig. 5.14). This is given by $\varepsilon = 3.22 \times 10^{-3} \tanh^2(1.26 \times 10^{-3}\zeta^{0.75})$.
3) The CERC (1977) growth curve, as presented by Young (1999, also shown in his Fig. 5.14). Here, the growth curve is $\varepsilon = 5.0 \times 10^{-3} \tanh^2(0.0125\chi^{0.42})$, and Young (1999) converts nondimensionalized fetch χ to nondimensionalized time ζ according to an expression from CERC (1977).
4) The final expression given by Kahma and Calkoen (1992), which is for the "composite dataset" with U_{10} normalization, $\varepsilon = 5.2 \times 10^{-7}\chi^{0.9}$. We convert the expression to nondimensionalized time ζ according to the same expression from CERC (1977), as mentioned above.

Pierson and Moskowitz's (1964) PM limit is also shown in Fig. 8, and is the total energy calculated from integration of the well-known PM spectrum given in that paper, as is done by KHH, which gives $\varepsilon_{PM} = 3.6 \times 10^{-3}$. The tabulated values of Moskowitz (1964) are also plotted, though it should be noted that, according to Moskowitz,

> the durations and fetches do not satisfy the theoretical requirement that they describe the time required and the distance needed to generate a fully developed sea starting from zero wave conditions. For the higher winds in particular, the tabulated values often represent the time and the distance for a sea raised to a given height by a wind of lesser velocity to grow to full development at the higher velocity.

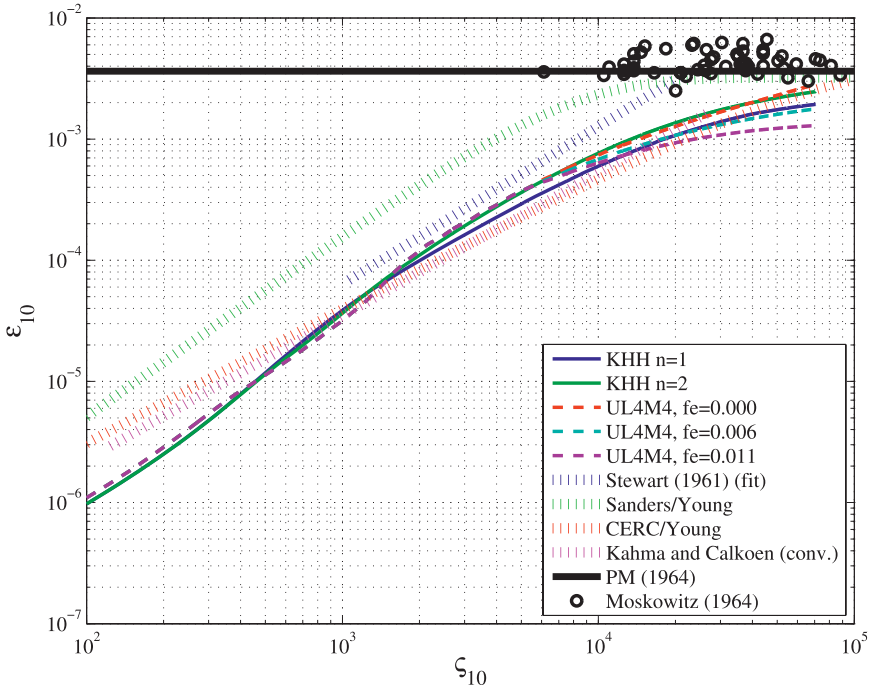

FIG. 8. Verification of duration-limited growth rate (energy vs time). Both quantities are nondimensionalized using U_{10}. Two models based on KHH, three new observation-consistent models (UL4M4), four empirical growth curves (described in the text), the PM limit and PM values are shown.

In other words, qualitatively, the plotted points should be shifted to the right in the figure, but quantitative means are not available. A similar warning could be made with regard to the Stewart (1961) linear fit.

An interesting outcome of the comparison is that the numerical models, including the KHH models, match each other much more closely than the empirical curves match each other. In some sense, this vindicates the calibration method, because had the Sanders (1976)/Young (1999) curve or Stewart (1961) linear fit been used, the calibration may have been unsuitable. On the other hand, the numerical models match the CERC (1977) and Kahma and Calkoen (1992) curves rather well.

The nonbreaking dissipation has a noticeable effect on energy predictions near full development. This comparison has implications for the treatment of the nonbreaking dissipation in the calibration: the models with nonbreaking dissipation appear to undershoot the Moskowitz values. This suggests that the preliminary calibration, which was created using $f_e = 0$, may lead to underprediction of energy near full development in subsequent, realistic simulation with nonzero f_e. This is easily addressed by considering alternate calibrations produced using nonzero f_e.

6. Discussion

In section 5, we looked at the ratio $R = D_{\text{tot}}/I_{\text{tot}} = \int S_{\text{ds}}(f)\,df / \int S_{\text{in}}(f)\,df$ as predicted by the single-point model, interpreted in the context of the observations as discussed by Donelan (1998). Given $N_{\text{tot}} = \int S_{\text{nl}}(f)\,df = 0$ for any model of the entire frequency range, the wave growth is controlled by $I_{\text{tot}} - D_{\text{tot}}$, which permits an infinite number of possible values for $R = D_{\text{tot}}/I_{\text{tot}}$. However, our implemented constraint on $\int [(S)_{\text{in}}(f)/C]\,df$ in Eq. (12) implies a soft constraint on I_{tot}, with some variation allowed because of the distribution of energy between slower and faster waves. (This variation resulting from C^{-1} can only be minor for a model that accurately predicts T_{m01}, T_p, and frequency width.) The effective constraint on I_{tot} implies that only minor variation in D_{tot} is allowed if the model is to predict wave height accurately (e.g., upper left panel in Fig. 3). Therefore, I_{tot} and D_{tot} are already essentially fixed without applying a constraint on R, and any model that does have a constraint on R would be overconstrained and thus would almost certainly fail to find a self-consistent solution. The modest discrepancy between the model-computed R values and the Donelan (1998) values suggest a shortcoming either in the implemented constraint (I_{tot}) or on the verification via Donelan's $D_{\text{tot}}/I_{\text{tot}}$ or in

the model calibration ($I_{tot} - D_{tot}$). This is left as a point for future inquiry.

As mentioned in section 2b, directional narrowness parameter A is set to unity in dissipation calculations (19), (21), and (22). Implementation of dependence of $S_{ds}(f)$ on directional spreading may be pursued in a later study by using $A \neq 1$. However, because the directional narrowness A will tend to decrease with increasing frequency in the spectral tail, this will reduce dissipation in the tail, which could present new problems in the context of the DBYB input term with its relatively strong forcing in that region. Further, with regard to (19) [the calculation for $E_T(f)$] Babanin (2009, see discussion of Fig. 5.28) has shown that the parameter is probably unnecessary in any model that includes cumulative dissipation.

The expression (6) is given by DBYB with $U = U_{10}$. However, it is desired that the model should scale with friction velocity U_* rather than U_{10}. The reader is referred to the concise summary of scaling arguments by KHH and the issue is discussed in greater detail by Alves et al. (2003). In earlier versions of our implementation, we used $U = 28U_*$ in (6), similar to the approach taken by KHH with the intention of forcing the model to scale with U_*. However, it was determined experimentally that this modification has insignificant impact on model results. The insensitivity is presumably due to the physical constraint on total stress, which is in terms of U_*, and applied after (6). Thus, for the representative wind speed, the present implementation as described in section 2 uses $U = U_{10}$, consistent with DBYB. The model nevertheless scales well with U_*, as mentioned in section 3.

As noted above, the DIA method is used to estimate the four-wave nonlinear interactions S_{nl} in simulations herein, even though the single-point model computations are certainly feasible with more complete approximations, such as those used by Tsagareli (2009), BY05 and YB06. This was done to provide consistency with a forthcoming manuscript, which will involve more expensive, two-dimensional applications. Also, we draw a distinction between foundation-building emphasis of those earlier works versus the present work with emphasis on practical, routine application. The less accurate nonlinear interaction computations in the present simulations, combined with the high-frequency limit of the prognostic spectrum of 1.0 Hz, implies that conclusions about the detailed behavior of the model physics should be regarded with suspicion until confirmed to also occur with more exact computations. For example, it will be shown in a subsequent manuscript that, in comparison to observations, bias in frequency spreading may be a common result from using the DIA.

The nonbreaking dissipation mechanism of Ardhuin et al. (2009) is used herein to represent the slow dissipation of nonbreaking waves, a situation represented in the model as $E(f) < E_T(f)$. The Ardhuin et al. method is based on momentum losses by the waves to the atmospheric boundary layer. Another theorized mode of energy loss is from turbulence generated by the nonbreaking orbital motion of waves (Babanin 2006). If the viscosity of water is not zero, then this turbulence must exist (Phillips 1961). This and other methods for accounting for nonbreaking dissipation will be evaluated and contrasted with the Ardhuin et al. method in a separate study.

The implications of the qualitative behavior demonstrated in Fig. 2 have been investigated thoroughly in numerical experiments here (e.g., Fig. 6), but this behavior can also be discussed in an intuitive context. When the ratio $E(f)/E_T(f)$ changes from 5 to 10, for example, as a result of current shear or by massive wind input, how should the model respond? The concave down model suggests that at $E(f)/E_T(f) = 5$ the dissipation $S_{ds}(f)$ is already near an asymptote and does not respond strongly when $E(f)/E_T(f)$ increases. The concave up models, on the other hand, suggest an explosive increase in $S_{ds}(f)$, especially for $L = 4$ (or $M = 4$). This scenario may be interpreted as being more physically plausible in situations where the wave energy must be destroyed within small time/space scales by some means, for example, in the surf zone, or in wave blocking situations.[5]

The cumulative dissipation term implemented in (22) represents only one of two apparent mechanisms for cumulative dissipation. Specifically, it represents the breaking of relatively short waves in the wake of or on top of large-wave breaking, triggered by the large breaker. However, it is recognized that there also exists a straining action, modulation of shortwave trains by the underlying large waves, which causes the shortwaves steepness to increase at the forward faces of longer waves, resulting in their frequent breaking (e.g., Unna 1941; Longuet-Higgins and Stewart 1960; Phillips and Banner 1974; Donelan et al. 2010). This type of dissipation is obviously distinct from (22) because it does not require that the longer waves are breaking, and it was in fact implemented experimentally in a previous version of SWAN, the so-called Cumulative Steepness Method (CSM; see van Vledder and Hurdle 2002; Hurdle and

[5] We point out, however, that none of these models have been extended for use in the surf zone, where it may be necessary to introduce new features to the dissipation formulation. The reader is referred to recent work on this topic by Filipot et al. (2010).

van Vledder 2004), where the dissipation is estimated from an integration of the steepness of longer waves

$$T_3(f,\theta) = a_3\left[\int_0^f k^2\varphi(f')E(f')\,df'\right]E(f,\theta), \quad (27)$$

where $\varphi(f')$ is a function to produce a dependency on the relative angle between $E(f, \theta)$ and the lower-frequency energy acting on it, $E(f',\theta')$. (In that earlier study, the CSM was implemented as the sole deep-water dissipation mechanism.) Prior observations of the suppression of wind sea by swell has primarily been for cases of steep swells in the laboratory (e.g., Phillips and Banner 1974), while in contrast it is difficult to detect the suppression in the open ocean (Violante-Carvalho et al. 2004) where swells are typically less steep. Further, it is possible that the suppression, when it does occur, may be due to the reduction of wind stress rather than enhanced breaking (Chen and Belcher 2000), in which case the additional dissipation term would not be appropriate. Therefore, it was decided that this third breaking mechanism should not be included in the present numerical model until observational studies provide clearer guidance.

7. Summary and conclusions

This paper introduces wind-input and whitecapping source terms consistent with key features observed experimentally by Banner et al. (2000), DBYB, BY05, and YB06. The source functions were initially developed by Tsagareli (2009), Tsagareli et al. (2010), and Babanin et al. (2010) and are adapted and improved here for practical application, and implemented in an experimental version of the SWAN model of Booij et al. (1999). The model development strategy is to rely on observational studies as much as is practical, as opposed to using theoretical works, such as Miles (1957) theory (section 1), as a starting point. Until now, these new observation-consistent terms with a number of significantly new physical features had not been tested in a two-dimensional model, and thus have not been available in a form that is usable in practical applications.

The new physics model is calibrated and evaluated using simple methods. The wind-input term is taken from DBYB, which is based on their observational work, and modified here by including a physical constraint on the total stress comparable to that of Tsagareli et al. (2010). Also, a drag coefficient formulation based on recent observational work is implemented. The calibration of the dissipation model herein is very limited, primarily concerned with model-to-model consistency rather than direct calibration against any particular observational dataset. However, the new dissipation function is observation consistent insofar as it conforms to two features of dissipation in the real ocean reported in the literature during the past decade. The first feature is that dissipation is two phase, with waves of any particular frequency dissipating due to either 1) the instability (and breaking) of waves of that frequency, or 2) the destabilization by larger breaking waves (e.g., through turbulence). The second feature is that wave breaking is thresholded, such that when the local spectral density falls below a spectral threshold derived from measurements, no breaking occurs at that frequency. Though they have been implemented separately in some fashion previously (section 1), these two features were not included together in any numerical model until very recently [e.g., Tsagareli (2009) in an academic model and Ardhuin et al. (2010) in WAVEWATCH III]. Both features contrast sharply with dissipation terms of the previous generation (e.g., Hasselmann 1974; KHH; WAMDI Group 1988; Booij et al. 1999) for which all waves are considered breaking all the time, and with all wave systems affecting the strength of dissipation of all other systems in a physically implausible manner (Rogers et al. 2003).

During the selection of calibration coefficients (a_1, a_2) for the new dissipation function, neither the frequency distribution (e.g., peak period, mean spectral period, frequency narrowness) nor the directional distribution (e.g., directional width) are considered. However, the dissipation formulation of Babanin et al. (2010) is generalized here, permitting variation in the degree or manner of sensitivity to the breaking threshold exceedence. Four variants (DL1M1, UL2M2, UL1M4, and UL4M4) are selected for evaluation here.

Though the primary intent of this paper is to introduce the new source functions as implemented in a practical model, the following conclusions can be made from the simple computations herein:

- The strong input to high-frequency waves by the new wind-input source function (DBYB) necessitates strong dissipation at these frequencies. The $\tilde{E}(f) = E(f)$ dissipation model, denoted DL1M1, insufficiently damps these waves.
- It is sufficient to treat the calibration coefficients of the new dissipation terms as constant, that is, independent of wave age. None necessitate complex calibrations, such as the lookup table procedure discussed in section 3.
- All four variants of the new model exhibit smaller ratios of integrated dissipation to integrated wind input $D_{\text{tot}}/I_{\text{tot}}$ than those reported by Donelan (1998). This indicates that the models retain a relatively larger portion of wind energy input than given by Donelan (1998). This discrepancy is being investigated in detail in a separate study.

- In comparisons that allow assessment of model quality, the three $\tilde{E}(f) = E_T(f)$ models—denoted UL2M2, UL1M4, and UL4M4—show very similar behavior, implying a surprisingly weak sensitivity to L and M in (21) and (22) (Figs. 3 and 7).
- The UL4M4 model adequately follows empirical temporal growth curves (Fig. 8), though the comparison also suggests that calibration may need to be updated to weaken breaking dissipation using wave observations and realistic simulations of large ocean basins with the nonbreaking dissipation included.
- The four models exhibit widely different distributions of inherent dissipation T_1 and induced dissipation T_2 with frequency, even when computed on identical parametric spectra. In such a comparison, the three $\tilde{E}(f) = E_T(f)$ models show strong sensitivity to L and M in (21) and (22) (Fig. 6). However, existing observations do not provide sufficient means to assess relative quality of these predictions. This highlights a challenge to address in further research.

In a forthcoming manuscript, we will further evaluate the three $\tilde{E}(f) = E_T(f)$ models using a variety of regional-scale hindcasts: cases representing pure wind sea, mixed sea/swell, hurricane, and slanting-fetch conditions.

Acknowledgments. The authors thank Dr. Stefan Zieger (Swinburne University) and anonymous reviewers for useful suggestions and comments on earlier drafts of this manuscript. The authors gratefully acknowledge support from the Office of Naval Research via the NRL Core Program (Program Element 61153N) and the National Ocean Partnership Program.

REFERENCES

Alves, J. H. G. M., and M. L. Banner, 2003: Performance of a saturation-based dissipation-rate source term in modeling the fetch-limited evolution of wind waves. *J. Phys. Oceanogr.,* **33,** 1274–1298.

——, ——, and I. R. Young, 2003: Revisiting the Pierson-Moskowitz asymptotic limits for fully developed wind waves. *J. Phys. Oceanogr.,* **33,** 1301–1323.

Ardhuin, F., F. Collard, B. Chapron, P. Queffeulou, J.-F. Filipot, and M. Hamon, 2008: Spectral wave dissipation based on observations: A global validation. *Proc. Chinese-German Joint Symp. on Hydraulics and Ocean Engineering,* Darmstadt, Germany, Universität Darmstadt, 391–400.

——, B. Chapron, and F. Collard, 2009: Observation of swell dissipation across oceans. *Geophys. Res. Lett.,* **36,** L06607, doi:10.1029/2008GL037030.

——, and Coauthors, 2010: Semi-empirical dissipation source functions for ocean waves. Part I: Definitions, calibration, and validations. *J. Phys. Oceanogr.,* **40,** 1917–1941.

Babanin, A. V., 2006: On a wave-induced turbulence and a wave-mixed upper ocean layer. *Geophys. Res. Lett.,* **33,** L20605, doi:10.1029/2006GL027308.

——, 2009: Breaking of ocean surface waves. *Acta Phys. Slovaca,* **59,** 305–535.

——, and Yu. P. Soloviev, 1987: Parameterization of width of directional energy distributions of wind-generated waves at limited fetches. *Izv. Atmos. Oceanic Phys.,* **23,** 645–651.

——, and ——, 1998: Variability of directional spectra of wind-generated waves, studied by means of wave staff arrays. *Mar. Freshwater Res.,* **49,** 89–101.

——, and I. R. Young, 2005: Two-phase behaviour of the spectral dissipation of wind waves. *Proc. Ocean Waves Measurement and Analysis, Fifth Intern. Symp. WAVES2005,* Madrid, Spain, CEDEX, Paper 51.

——, and A. J. van der Westhuysen, 2008: Physics of ''saturation-based'' dissipation functions proposed for wave forecast models. *J. Phys. Oceanogr.,* **38,** 1831–1841.

——, I. R. Young, and M. L. Banner, 2001: Breaking probabilities for dominant surface waves on water of finite constant depth. *J. Geophys. Res.,* **106** (C6), 11 659–11 676.

——, M. L. Banner, I. R. Young, and M. A. Donelan, 2007a: Wave follower measurements of the wind input spectral function. Part III: Parameterization of the wind input enhancement due to wave breaking. *J. Phys. Oceanogr.,* **37,** 2764–2775.

——, K. N. Tsagareli, I. R. Young, and D. Walker, 2007b: Implementation of new experimental input/dissipation terms for modeling spectral evolution of wind waves. *Proc. 10th Int. Workshop on Wave Hindcasting and Forecasting and Coastal Hazards,* Oahu, HI, U.S. Army Engineer Research and Development Center's Coastal and Hydraulics Laboratory, Environment Canada, and WMO/IOC Joint Technical Commission for Oceanography and Marine Meteorology. [Available online at ftp://www.wmo.int/Documents/PublicWeb/amp/mmop/documents/JCOMM-TR/J-TR-44/WWW/Papers/BTYW_2007_10th_Int_Workshop_Wave_Hindcasting_Forecasting_a_.pdf.]

——, ——, ——, and D. J. Walker, 2010: Numerical investigation of spectral evolution of wind waves. Part II: Dissipation function and evolution tests. *J. Phys. Oceanogr.,* **40,** 667–683.

Banner, M. L., and W. L. Peirson, 1998: Tangential stress beneath wind-driven air-water interfaces. *J. Fluid Mech.,* **364,** 115–145.

——, and R. P. Morison, 2010: Refined source terms in wind wave models with explicit wave breaking prediction. Part I: Model framework and validation against field data. *Ocean Modell.,* **33,** 177–189.

——, A. V. Babanin, and I. R. Young, 2000: Breaking probability for dominant waves on the sea surface. *J. Phys. Oceanogr.,* **30,** 3145–3160.

——, J. R. Gemmrich, and D. M. Farmer, 2002: Multi-scale measurements of ocean wave breaking probability. *J. Phys. Oceanogr.,* **32,** 3364–3375.

Battjes, J. A., and G. P. van Vledder, 1984: Verification of Kimura's theory for wave group statistics. *Proc. of the 19th Int. Conf. Coastal Engineering,* Houston, TX, ASCE, 642–648.

Booij, N., R. C. Ris, and L. H. Holthuijsen, 1999: A third-generation wave model for coastal regions 1. Model description and validation. *J. Geophys. Res.,* **104** (C4), 7649–7666.

CERC, 1977: Shore protection manual. U.S. Army Coastal Research Center, Vols. 1–3.

Chen, G., and S. E. Belcher, 2000: Effects of long waves on wind-generated waves. *J. Phys. Oceanogr.,* **30,** 2246–2256.

Donelan, M. A., 1998: Air-water exchange processes. *Physical Processes in Lakes and Oceans,* J. Imberger, Ed., Coastal and Estuarine Studies, Vol. 54, Amer. Geophys. Union, 19–36.

——, J. Hamilton, and W. H. Hui, 1985: Directional spectra of wind-generated waves. *Philos. Trans. Roy. Soc.,* **A315,** 509–562.

——, A. V. Babanin, I. R. Young, M. L. Banner, and C. McCormick, 2005: Wave follower field measurements of the wind input spectral function. Part I: Measurements and calibrations. *J. Atmos. Oceanic Technol.,* **22,** 799–813.

——, ——, ——, and ——, 2006: Wave follower field measurements of the wind input spectral function. Part II: Parameterization of the wind input. *J. Phys. Oceanogr.,* **36,** 1672–1688.

——, B. K. Haus, W. J. Plant, and O. Troianowski, 2010: Modulation of short wind waves by long waves. *J. Geophys. Res.,* **115,** C10003, doi:10.1029/2009JC005794.

Ewans, K. C., and A. C. Kibblewhite, 1990: An examination of fetch-limited wave growth off the west coast of New Zealand by a comparison with JONSWAP results. *J. Phys. Oceanogr.,* **20,** 1278–1296.

Filipot, J.-F., F. Ardhuin, and A. V. Babanin, 2010: A unified deep-to-shallow water wave-breaking probability parameterization. *J. Geophys. Res.,* **115,** C04022, doi:10.1029/2009JC005448.

Forristall, G. Z., 1981: Measurements of a saturation range in ocean wave spectra. *J. Geophys. Res.,* **86** (C9), 8075–8084.

Hasselmann, K., 1974: On the spectral dissipation of ocean waves due to white capping. *Bound.-Layer Meteor.,* **6,** 107–127.

Hasselmann, S., K. Hasselmann, J. H. Allender, and T. P. Barnett, 1985: Computations and parameterizations of the nonlinear energy transfer in a gravity-wave spectrum. Part II: Parameterizations of the nonlinear energy transfer for application in wave models. *J. Phys. Oceanogr.,* **15,** 1378–1391.

Hsu, C. T., E. Y. Hsu, and R. L. Street, 1981: On the structure of turbulent flow over a progressive water wave: Theory and experiment in a transformed, wave-following co-ordinate system. *J. Fluid Mech.,* **105,** 87–117.

——, H. W. Wu, E. Y. Hsu, and R. L. Street, 1982: Momentum and energy transfer in wind generation of waves. *J. Phys. Oceanogr.,* **12,** 929–951.

Hurdle, D. P., and G. Ph. van Vledder, 2004: Improved spectral wave modeling of white-capping dissipation in swell sea systems. *Proc. 23rd Int. Conf. on Offshore Mechanics and Arctic Engineering,* Vancouver, BC, Canada, ASME, 539–544.

Hwang, P. A., 2011: A note on the ocean surface roughness spectrum. *J. Atmos. Oceanic Technol.,* **28,** 436–443.

——, and D. W. Wang, 2001: Directional distributions and mean square slopes in the equilibrium and saturation ranges of the wave spectrum. *J. Phys. Oceanogr.,* **31,** 1346–1360.

Janssen, P. A. E. M., 1989: Wave-induced stress and the drag of air flow over sea waves. *J. Phys. Oceanogr.,* **19,** 745–754.

——, 1991: Quasi-linear theory of wind-wave generation applied to wave forecasting. *J. Phys. Oceanogr.,* **21,** 1631–1642.

Jarosz, E., D. A. Mitchell, D. W. Wang, and W. J. Teague, 2007: Bottom-up determination of air-sea momentum exchange under a major tropical cyclone. *Science,* **315,** 1707–1709.

Kahma, K. K., and C. J. Calkoen, 1992: Reconciling discrepancies in the observed growth of wind-generated waves. *J. Phys. Oceanogr.,* **22,** 1389–1405.

Komen, G. J., S. Hasselmann, and K. Hasselmann, 1984: On the existence of a fully developed wind-sea spectrum. *J. Phys. Oceanogr.,* **14,** 1271–1285.

Longuet-Higgins, M. S., and R. W. Stewart, 1960: Changes in the form of short gravity waves on long waves and tidal currents. *J. Fluid Mech.,* **8,** 564–585.

Manasseh, R., A. V. Babanin, C. Forbes, K. Rickards, I. Bobevski, and A. Ooi, 2006: Passive acoustic determination of wave-breaking events and their severity across the spectrum. *J. Atmos. Oceanic Technol.,* **23,** 599–618.

Miles, J. W., 1957: On the generation of surface waves by shear flows. *J. Fluid Mech.,* **3,** 185–204.

Moskowitz, L., 1964: Estimates of the power spectrums for fully developed seas for wind speeds of 20 to 40 knots. *J. Geophys. Res.,* **69** (24), 5161–5179.

Phillips, O. M., 1961: A note on the turbulence generated by gravity waves. *J. Geophys. Res.,* **66** (9), 2889–2893.

——, 1984: On the response of short ocean wave components at a fixed number to ocean current variations. *J. Fluid Mech.,* **14,** 1425–1433.

——, and M. L. Banner, 1974: Wave breaking in the presence of wind drift and swell. *J. Fluid Mech.,* **66,** 625–640.

Pierson, W. J., and L. Moskowitz, 1964: A proposed spectral form for fully developed wind seas based on the similarity theory of S. A. Kitaigorodskii. *J. Geophys. Res.,* **69** (24), 5181–5190.

Powell, M. D., P. J. Vickery, and T. A. Reinhold, 2003: Reduced drag coefficient for high speeds in tropical cyclones. *Nature,* **422,** 279–283.

Rogers, W. E., P. A. Hwang, and D. W. Wang, 2003: Investigation of wave growth and decay in the SWAN model: Three regional-scale applications. *J. Phys. Oceanogr.,* **33,** 366–389.

Sanders, J. W., 1976: A growth-stage scaling model for the wind-driven sea. *Dtsch. Hydrogr. Z.,* **29,** 136–161.

Snyder, R. L., F. W. Dobson, J. A. Elliot, and R. B. Long, 1981: A field study of wind generation of ocean waves. *J. Fluid Mech.,* **102,** 1–59.

Stewart, R. W., 1961: The wave drag of wind over water. *J. Fluid Mech.,* **10,** 189–194.

SWAN Team, 2010: SWAN scientific and technical documentation. SWAN cycle III version 40.81, Delft University of Technology, 118 pp. [Available online at http://www.swan.tudelft.nl.]

Tolman, H. L., 2009: User manual and system documentation of WAVEWATCH III Version 3.14. NCEP Tech. Note, 220 pp. [Available online at http://polar.ncep.noaa.gov/mmab/papers/tn276/MMAB_276.pdf.]

——, 1991: A third-generation model for wind-waves on slowly varying, unsteady, and inhomogeneous depths and currents. *J. Phys. Oceanogr.,* **21,** 782–797.

——, and D. Chalikov, 1996: Source terms in a third-generation wind wave model. *J. Phys. Oceanogr.,* **26,** 2497–2518.

Tsagareli, K. N., 2009: Numerical investigation of wind input and spectral dissipation in evolution of wind waves. Ph.D. thesis, University of Adelaide, 217 pp.

——, A. V. Babanin, D. J. Walker, and I. R. Young, 2010: Numerical investigation of spectral evolution of wind waves. Part I: Wind input source function. *J. Phys. Oceanogr.,* **40,** 656–666.

Unna, P. J. H., 1941: White horses. *Nature,* **148,** 226–227.

van der Westhuysen, A. J., 2007: Advances in the spectral modeling of wind waves in the Nearshore. Ph.D. thesis. Delft University of Technology, 206 pp.

——, M. Zijlema, and J. A. Battjes, 2007: Nonlinear saturation-based whitecapping dissipation in SWAN for deep and shallow water. *Coastal Eng.,* **54,** 151–170.

van Vledder, G. P., 2002: A subroutine version of the Webb/Resio/Tracy method for the computation of nonlinear quadruplet wave-wave interactions in deep and shallow water. Alkyon Rep. 151b, 55 pp.

——, 2006: The WRT method for computation of non-linear four-wave interactions in discrete spectral wave models. *Coastal Eng.,* **53,** 223–242.

——, and D. P. Hurdle, 2002: Performance of formulations for whitecapping in wave prediction models. *Proc. Int. Conf. on Ocean, Offshore and Arctic Eng. (OMAE) 2002,* Oslo, Norway, ASME, 155–163.

Violante-Carvalho, N., F. J. Ocampo-Torres, and I. S. Robinson, 2004: Buoy observations of the influence of swell on wind waves in the open ocean. *Appl. Ocean Res.,* **26,** 49–60.

WAMDI Group, 1988: The WAM model—A third-generation ocean wave prediction model. *J. Phys. Oceanogr.,* **18,** 1775–1810.

The WISE Group, 2007: Wave modelling—The state of the art. *Prog. Oceanogr.,* **75,** 603–674.

Wu, J., 1982: Wind stress coefficients over sea surface from breeze to hurricane. *J. Geophys. Res.,* **87** (C12), 9704–9706.

Young, I. R., 1999: *Wind Generated Ocean Waves*. Elsevier, 288 pp.

——, and A. V. Babanin, 2006: Spectral distribution of energy dissipation of wind-generated waves due to dominant wave breaking. *J. Phys. Oceanogr.,* **36,** 376–394.